Statistical Study of Betatron and Fermi Electron Acceleration at Dipolarization Fronts

Citation for the original published paper (version of record):
Kolokotronis, A., Graham, D., Khotyaintsev, Y. et al (2026). Statistical Study of Betatron and Fermi Electron Acceleration at Dipolarization Fronts. Geophysical Research Letters, 53(15).
http://dx.doi.org/10.1029/2026GL122885

AGU ADVANCING EARTH AND SPACE SCIENCES

Geophysical Research Letters®

RESEARCH LETTER
10.1029/2026GL122885

Statistical Study of Betatron and Fermi Electron Acceleration at Dipolarization Fronts

A. Kolokotronis[1,2], **D. B. Graham**[1], **Yu. V. Khotyaintsev**[1,2], **C. Norgren**[1,3], **K. Steinvall**[4], **and L. Richard**[1]

[1]Swedish Institute of Space Physics, Uppsala, Sweden, [2]Space and Plasma Physics, Department of Physics and Astronomy, Uppsala University, Uppsala, Sweden, [3]University of Bergen, Bergen, Norway, [4]Department of Physics, Chalmers University of Technology, Gothenburg, Sweden

Key Points:

- Betatron acceleration locally heats pre-existing plasma sheet electrons, ahead of dipolarization fronts
- Fermi acceleration is potentially contributing to the energization of outflow electrons up to 100 s keV, behind the fronts
- Betatron acceleration increases farther tailward, near the most probable X-line, while Fermi acceleration intensifies near Earth's dipole

Supporting Information:

Supporting Information may be found in the online version of this article.

Correspondence to:

A. Kolokotronis,
apostolosk@irf.se

Citation:

Kolokotronis, A., Graham, D. B., Khotyaintsev, Y. V., Norgren, C., Steinvall, K., & Richard, L. (2026). Statistical study of betatron and fermi electron acceleration at dipolarization fronts. *Geophysical Research Letters*, *53*, e2026GL122885. https://doi.org/10.1029/2026GL122885

Received 15 APR 2026
Accepted 21 JUL 2026

Author Contributions:

Conceptualization: A. Kolokotronis, D. B. Graham
Data curation: A. Kolokotronis, D. B. Graham, Yu. V. Khotyaintsev, L. Richard
Formal analysis: A. Kolokotronis, D. B. Graham, Yu. V. Khotyaintsev, C. Norgren, K. Steinvall, L. Richard
Funding acquisition: D. B. Graham, Yu. V. Khotyaintsev
Investigation: A. Kolokotronis, D. B. Graham, Yu. V. Khotyaintsev, C. Norgren, K. Steinvall, L. Richard

Abstract

Magnetic reconnection jets in Earth's magnetotail are regions of electron heating and acceleration. They are often associated with dipolarization fronts (DFs), which are characterized by sharp increases in the northward magnetic field component B_z. Electrons can be accelerated at DFs mainly through the betatron and Fermi mechanisms. We perform a statistical study of betatron and Fermi electron rate of energy change at Earthward-propagating DFs observed by the Magnetospheric Multiscale (MMS) spacecraft. Our results show that betatron acceleration is dominant ahead of DFs, where suprathermal electron fluxes perpendicular to the magnetic field are detected. Up to ∼20 ion inertial lengths inside the outflow, Fermi acceleration acts on the low-density electron population, potentially driving them to high energies (∼100 keV). Spatially in the magnetotail, betatron acceleration is statistically larger near the most probable X-line location, while Fermi-dominated events are observed closer to the Earth.

Plain Language Summary

Magnetic reconnection in Earth's magnetotail is a process that reconfigures the magnetic field topology and generates fast plasma outflows (jets). Electrons can be heated and accelerated to near-relativistic energies at the leading edges of these outflows, known as dipolarization fronts (DFs). Electrons at DFs are accelerated mainly by the betatron and Fermi acceleration mechanisms, perpendicular and parallel to the background magnetic field, respectively, though their relative contributions are not fully understood. Using data from the Magnetospheric Multiscale (MMS) mission, we quantify the rate of electron energy change due to these two mechanisms for a database of DFs, and study their spatial distribution around the DF and in different regions of the magnetotail. We find betatron acceleration to be important for locally accelerating electrons ahead of DFs, and significant early in the outflow's propagation through the magnetotail. On the other hand, Fermi acceleration is acting inside the outflow, potentially being responsible for the high-energy electrons observed there, especially as the jets approach Earth's dipole field. Our results suggest that betatron and Fermi acceleration can each dominate at different stages of the jet's evolution.

1. Introduction

Magnetic reconnection is a fundamental process in astrophysical, solar, and laboratory plasmas, converting magnetic energy to bulk flow kinetic energy and plasma heating. In Earth's magnetotail reconnection, plasma heating and acceleration occur at the reconnection region (Birn et al., 2013), and during the outflow transport (Ashour-Abdalla et al., 2011; Xu et al., 2018). Transient reconnection outflows known as bursty bulk flows (BBFs) (Angelopoulos et al., 1992) transport plasma and reconnected magnetic flux both Earthward and tailward. BBFs are a result of unsteady reconnection (Sitnov et al., 2009) and often have sharp magnetic field structures at their leading edges, called dipolarization fronts (DFs) (Nakamura et al., 2002). In spacecraft data, DFs appear as steep increases in the magnetic field component normal to the neutral plasma sheet (PS) (B_z) (Fu et al., 2012; Runov et al., 2011). They are ion-scale boundaries (Schmid et al., 2011) generated when field lines carried by the tenuous plasma in the reconnection jet pile up against the denser pre-existing PS. Electrons with energies up to ∼100 s keV (Fu et al., 2013; Runov et al., 2011; Wei et al., 2023), and waves changing the electron distribution function through acceleration and/or scattering of electron pitch-angles (Khotyaintsev et al., 2011; S. Y. Huang et al., 2015) have been reported around DFs. These observations indicate that DFs can be efficient converters of kinetic energy and Poynting flux into heating and electron acceleration.

Methodology: A. Kolokotronis, D. B. Graham, Yu. V. Khotyaintsev, C. Norgren, K. Steinvall, L. Richard
Project administration: D. B. Graham, Yu. V. Khotyaintsev
Resources: D. B. Graham, Yu. V. Khotyaintsev, L. Richard
Software: A. Kolokotronis, D. B. Graham, Yu. V. Khotyaintsev, L. Richard
Supervision: D. B. Graham, Yu. V. Khotyaintsev, C. Norgren, K. Steinvall
Validation: A. Kolokotronis, D. B. Graham, Yu. V. Khotyaintsev, C. Norgren, K. Steinvall, L. Richard
Visualization: A. Kolokotronis
Writing – original draft: A. Kolokotronis
Writing – review & editing: D. B. Graham, Yu. V. Khotyaintsev, C. Norgren, K. Steinvall, L. Richard

Different mechanisms are known to contribute to electron acceleration at DFs. These mechanisms and their contribution at different stages of the jets' evolution (Birn et al., 2004; K. Huang et al., 2021) are responsible for the variety of observed pitch-angle distributions (PADs) in the vicinity of DFs. The conservation of the magnetic moment ($\mu = \mathcal{E}_\perp / B$, where $B = |\mathbf{B}|$ is the magnetic field magnitude and $\mathcal{E}_\perp$ is the electron kinetic energy perpendicular to **B**) as electrons encounter the increased magnetic field at the front leads to betatron acceleration perpendicular to the field lines, and pancake-like (electrons at $\sim 90°$ pitch-angle) PADs (Fu et al., 2011; Wei et al., 2023). Parallel Fermi acceleration (Birn et al., 2012; Northrop, 1963) occurs when the electron parallel momentum, $p_\parallel$, increases, as the second adiabatic invariant, $J = \oint p_\parallel ds$ is conserved in shortened field lines (type A), or when electrons cross or bounce at the neutral sheet (type B). A result of Fermi acceleration is the generation of cigar (electrons around 0° and 180° pitch-angles) PADs (Fu et al., 2011). The combination of betatron and Fermi acceleration can be associated with the more complex rolling-pin (electrons around 0°, 90° and 180° pitch-angles) PADs that have been observed both ahead (Xing et al., 2023) and behind (Liu et al., 2017) DFs.

Both Fermi and betatron acceleration have been shown to be more important than acceleration by parallel to **B** electric fields $(E_\parallel)$ at DFs (Dahlin et al., 2014, 2016; Ma et al., 2020, 2022). Betatron acceleration has been found to occur in magnetotail dipolarizations associated with substorm onsets (Asano et al., 2010), accelerating electrons up to $\sim$100 keV (Malykhin et al., 2018; Turner et al., 2016). Field-aligned electron populations during other such dipolarizations have been interpreted as Fermi accelerated electrons (Smets et al., 1999). Other studies have shown that both mechanisms are necessary to account for the observed high-energy electron PADs (Pan et al., 2012; Tang et al., 2021).

Even though the betatron and Fermi acceleration mechanisms have been quantified for individual DFs (Wei et al., 2023), and in statistical studies (Ma et al., 2020), their spatial extent around the DF boundary, their importance in different magnetotail regions, and their relative contribution to extreme electron acceleration up to 100 s keV (Fu et al., 2013; Wei et al., 2023) are still not fully understood. In this study, we quantify these two electron acceleration mechanisms around DFs using data from the Magnetospheric Multiscale (MMS) mission and compare them to observations of thermal and high-energy electron fluxes and their anisotropies. We examine their relative importance with respect to the DF boundary, therefore assessing the local contribution of betatron and Fermi acceleration on electrons of the non-reconnecting pre-existing PS (ahead of the DF) and on those convecting with the reconnection outflow (behind the DF). We also examine their spatial distribution in the magnetotail as a function of distance from Earth and the center of the PS.

2. Data Sets

We use data from the MMS spacecraft (Burch et al., 2016) during the magnetotail seasons of May–August 2017 and June 2018. A database of BBFs with DFs characterized by single, sharp B_z increases, compiled by Richard et al. (2022), is used. We use burst-mode magnetic field (8 ms) measurements from the Flux Gate Magnetometer (Russell et al., 2016) and electric field (0.1 ms) from the Electric field Double Probes (EDP) (Ergun et al., 2016; Lindqvist et al., 2016). Ion bulk velocities are calculated by the Fast Plasma Investigation (FPI) (Pollock et al., 2016) Dual Ion Spectrometer (150 ms) and the Hot Plasma Composition Analyzer (HPCA) (10 s)(Young et al., 2016). The latter is used because FPI (up to 31.2 keV) often does not cover the energy ranges of ions encountered in the PS, resulting in underestimated flow speeds, whereas HPCA detects ions up to $\sim$40 keV. Electron omnidirectional fluxes, PADs, and moments are calculated from the FPI Dual Electron Spectrometer (DES) measurements, with a cadence of 30 ms. We use partial electron moments for energies above 100 eV to exclude photoelectrons from the spacecraft (Gershman et al., 2017). For high-energy electrons, we use measurements from the Fly's Eye Energetic Particle Spectrometer (FEEPS) (Blake et al., 2016), with a cadence of 300 ms, which we correct for sun contamination (Burch et al., 2024) (see text S1 and Figures S1 and S2 in Supporting Information S1). All data used in this study are in the Geocentric Solar Magnetic coordinate system.

The separations between the MMS spacecraft ($\sim$10 km) are comparable to typical electron gyroradii in the PS for typical values of $B = 10$ nT and $\mathcal{E}_\perp = 1$ keV, $\rho_e = \frac{m_e v_\perp}{eB} = 11$ km where m_e is the electron mass, $v_\perp$ is the electron velocity perpendicular to **B** and e is the electron charge. The measurements from the four spacecraft are thus similar. Therefore, we can take four-spacecraft averages and compute spatial derivatives of measured quantities. For FEEPS, we combine the energy channels from the four spacecraft in the way shown in Figure S3 in Supporting Information S1.

3. Case Studies of Electron Acceleration

3.1. Acceleration in the Guiding Center Approximation

To quantify the rate of electron kinetic energy density change (units of power density) due to the Fermi (W_F) and betatron (W_b) mechanisms, the guiding center approximation is used (Dahlin et al., 2014; Northrop, 1963):

$$W_b = \frac{P_\perp}{B}\left(\frac{\partial B}{\partial t} + \mathbf{u}_E \cdot \nabla B\right)$$
$$W_F = \left(P_\| + m_e n_e u_\|^2\right)\mathbf{u}_E \cdot \boldsymbol{\kappa}_{curv} \tag{1}$$

where $\mathbf{B}$ and $\mathbf{E}$ are the magnetic and electric field, $\mathbf{u}_E = (\mathbf{E} \times \mathbf{B})/B^2$ is the $\mathbf{E} \times \mathbf{B}$ drift velocity, $\boldsymbol{\kappa}_{curv} = \mathbf{b} \cdot \nabla \mathbf{b}$ is the curvature of $\mathbf{B}$ with $\mathbf{b} = \mathbf{B}/B$, m_e is the electron mass, n_e is the electron number density, $P_\perp$, $P_\|$ are the electron pressures perpendicular and parallel to $\mathbf{B}$, and $u_\|$ is the electron bulk velocity parallel to $\mathbf{B}$. The uncertainties in W_b and W_f are given by (Zhong et al., 2020):

$$\delta W_b = (P_\perp + \delta P_\perp)\,\frac{\mathbf{b} \times (\nabla B + \delta \nabla B)}{B^2} \cdot (\mathbf{E}_\perp + \delta \mathbf{E}_\perp)$$
$$\delta W_F = \left(P'_\| + \delta P'_\|\right)\frac{\mathbf{B} \times \left[\frac{\mathbf{B} \cdot \nabla \mathbf{B}}{B^2} + \frac{\mathbf{B} \cdot \delta \nabla \mathbf{B}}{B^2}\right]}{B^2} \cdot (\mathbf{E}_\perp + \delta \mathbf{E}_\perp) \tag{2}$$

where $P'_\| = P_\| + m_e n_e u_\|^2$ and $\mathbf{E}_\perp$ is the electric field perpendicular to $\mathbf{B}$. Dividing W_b and W_F (Equation 1) by n_e, we obtain the rate of energy change (units of power) per electron, due to betatron ($w_b = W_b/n_e$) and Fermi ($w_F = W_F/n_e$) acceleration, respectively.

For the acceleration terms calculated using the guiding-center approximation (Equation 1) to be applicable, electrons must remain adiabatic, and therefore conserve their magnetic moment. The change in μ is $\Delta\mu/\mu \sim \exp\left(-2\kappa^2/3\right)$ (Birmingham, 1984), for $\kappa \gg 1$, where κ is the adiabaticity parameter (Büchner & Zelenyi, 1989):

$$\kappa = \sqrt{\frac{r_{curv}}{\rho_e}} \tag{3}$$

where $r_{curv} = |\boldsymbol{\kappa}_{curv}|^{-1}$ is the magnetic field curvature radius. As κ decreases, $\Delta\mu/\mu$ increases, and the electron motion is no longer adiabatic when κ approaches 1. In this limit, Equation 1 is not applicable (Steinvall et al., 2025).

3.2. Data Processing

Here, we present the details of the Fermi and betatron acceleration terms (Equation 1) and κ (Equation 3) calculations. To calculate the gradient and curvature of the magnetic field in Equation 1, as well as r_{curv} in Equation 3, we use four-spacecraft methods (Dunlop et al., 2002). To smooth $\mathbf{B}$, we apply a moving average, with a $\sim$900 ms window, less than typical DF timescales ((Fu et al., 2012) and see Section 4.1). A five-point stencil time derivative is implemented to calculate $\frac{\partial B}{\partial t}$. All quantities are resampled to the DES burst-mode cadence (30 ms). Using four-spacecraft averages of quantities in Equation 1, we quantify w_b and w_F along the path of the MMS tetrahedron.

3.3. Results

In Figure 1, we present overviews of two DFs, characterized by moderate (DF1, left) and high (DF2, right) electron energization. Behind DF2, the omnidirectional differential particle flux as measured by FEEPS, is enhanced up to energies $\sim$200 keV (Figure 1d2), while behind DF1 (Figure 1d1) the flux is enhanced only up to $\sim$100 keV. We observe an increase in B_z (Figures 1a1 and 1a2), a drop in electron density n_e (Figures 1b1 and 1b2) around the time

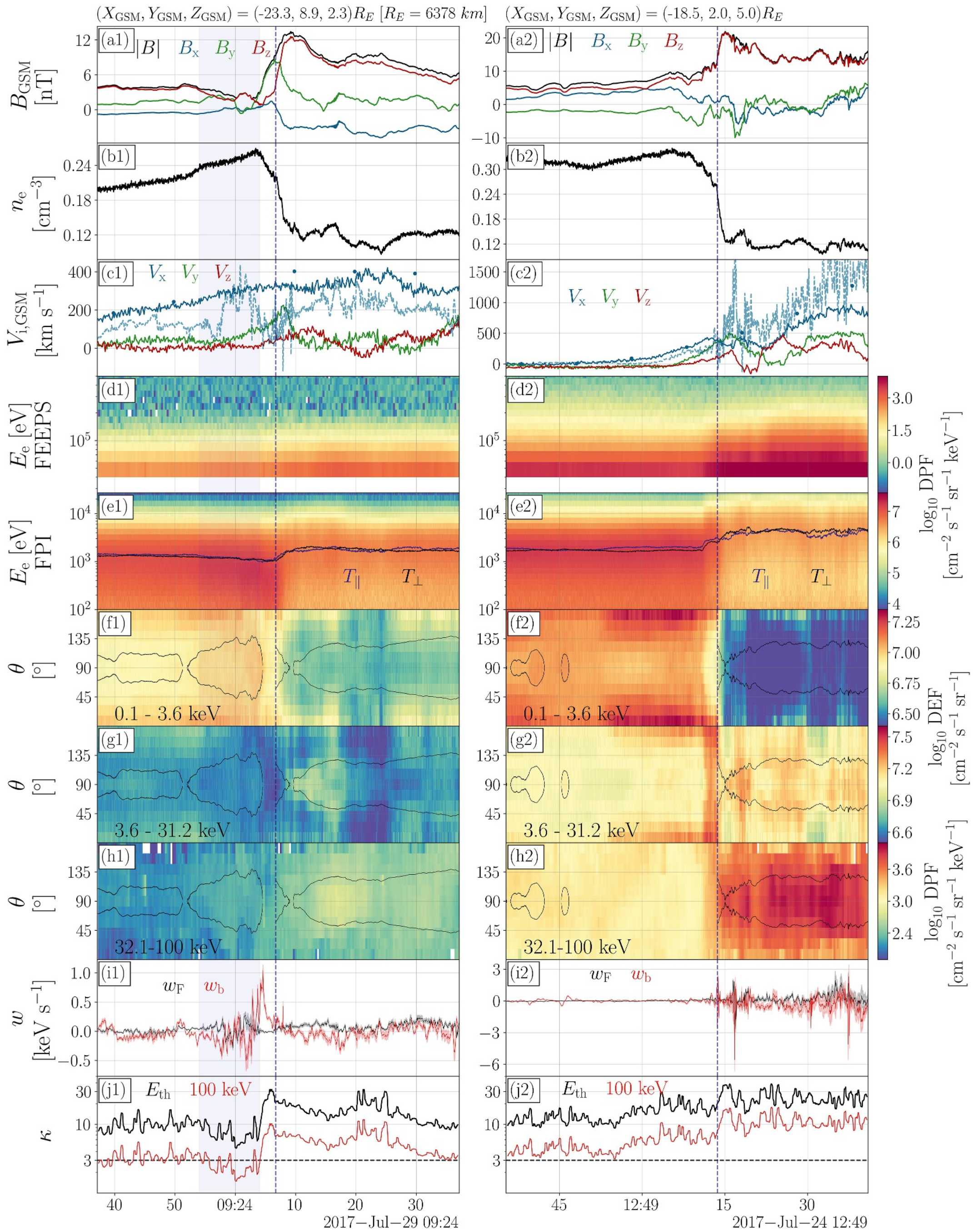

Figure 1. Overview of low (DF1, left) and high (DF2, right) electron energization DFs. (a1–a2) Magnetic field in geocentric solar magnetic (GSM). (b1–b2) Electron number density. (c1–c2) Ion bulk velocity in GSM from fast plasma investigation (FPI) (solid lines), $V_{i,x}$ from hot plasma composition analyzer (blue circles), and the x–component of the $\mathbf{E} \times \mathbf{B}$ drift velocity (dashed blue lines). (d1–d2) Electron omnidirectional differential particle fluxes from fly's eye energetic particle spectrometer (FEEPS). (e1–e2) Electron omnidirectional differential particle fluxes from FPI, perpendicular (black) and parallel (blue) temperatures. (f1–f2) FPI 0.1–3.6 keV electron pitch–angle distribution (PAD). (g1–g2) FPI 3.6–31.2 keV electron PAD. (h1–h2) FEEPS 32.1–100 keV electron PAD. Trapped electron pitch–angles are within the areas marked with black lines in panels (f1–h1) and (f2–h2). (i1–i2) Rate of electron energy change due to betatron (red) and Fermi (black) acceleration and their uncertainties (Equation 2, shaded areas). (j1–j2) The adiabaticity parameter for thermal energy (black) and 100 keV (red) electrons. The black dashed line indicates the threshold, above which electrons are adiabatic. Blue dashed lines indicate the time of the maximum $\partial B_z/\partial t$. The magnetic dip interval ahead of DF1 is marked with the blue shaded area.

of maximum $\frac{\partial B_z}{\partial t}$ (blue vertical dashed line), as well as fast Earthward ion flows (Figures 1c1 and 1c2), which are characteristic of DFs. At DF1, we see a moderate increase in the flow speed (maximum of ~ 400 km s^{-1}) across the DF, whereas in DF2, the flow speed reaches values of ~ 1300 km s^{-1} as indicated by the HPCA proton velocity (blue dots) and $\mathbf{u}_{E,x}$ (blue dashed line).

Electron temperatures both parallel and perpendicular to $\mathbf{B}$, and suprathermal electron fluxes measured by FPI (Figures 1e1 and 1e2) increase in the outflows behind both DFs, similar to the FEEPS observations. Behind both DFs, electrons around thermal energies mostly move along the dipolarized field lines, as seen in the PAD spectrogram in Figures 1f1 and 1f2. In contrast, at suprathermal energies, there is an increase in perpendicular electrons, observed by both FPI (Figures 1g1 and 1g2) and FEEPS (Figures 1h1 and 1h2). We note that we cannot compare the perpendicular and parallel fluxes from FEEPS, since the field-of-view of the detectors makes it challenging to detect electrons along the MMS spin axis direction, which is near-field-aligned for large B_z.

Thermal energy electrons (E_{th}) are adiabatic ($\kappa > 3$, in Figures 1j1 and 1j2), corresponding to $\Delta\mu/\mu < 2 \times 10^{-3}$. Therefore, Equation 1 is applicable. Additionally, the uncertainties in w_b and w_F (shaded areas in Figures 1i1 and 1i2) are small, particularly at the peak values of the two terms, suggesting the calculated values are reliable. Electrons at 100 keV are mostly adiabatic close to both DFs, but the guiding center approximation could break ahead of DF1, where $\kappa_{\min} \approx 1.5$ ($\Delta\mu/\mu = 0.22$).

Ahead of DF1, both betatron cooling ($w_b < 0$) and heating ($w_b > 0$) are observed (Figure 1i1) around the magnetic dip (Runov et al., 2011), where the magnetic field magnitude decreases and subsequently increases. Behind the DF, betatron cooling is observed, while w_F is mostly positive. At high energies, fluxes of electrons around perpendicular pitch-angles increase in the same region (Figure 1h1), despite the betatron cooling, indicating that their injection into perpendicular directions occurred earlier or somewhere else in the outflow.

In the magnetic dip region, there is an increase in flux of electrons around 90° pitch-angle (Figure 1f1). This increase could be due to the betatron acceleration of electrons trapped locally ahead of DF1. Assuming conservation of the magnetic moment and energy, the change in pitch-angle is given by (Baumjohann & Treumann, 2006):

$$\theta_{\mathrm{tr}} = \sin^{-1}\sqrt{\frac{B}{B_0}} \quad (4)$$

for an electron that mirrors at B_0. Suprathermal electrons (Figures 1f1–1h1) ahead of DF1 (at 09:23:54–09:24:04, blue shaded area in Figures 1a1–1j1) are bounded by the predicted pitch-angle variation, suggesting they are trapped in this region. Here, w_b has a negative (betatron cooling) peak of $\sim$–0.5 keV s^{-1} and becomes positive (betatron heating) just before the DF. The mean acceleration terms over this interval are $\langle w_b \rangle = -0.1$ keV s^{-1} and $\langle w_F \rangle = 0.04$ keV s^{-1}. Therefore, trapped electrons ahead of DF1 would experience a deceleration in the perpendicular direction ($w_b < 0$) and field-aligned acceleration ($w_F > 0$).

For DF2, w_b and w_F are smaller ahead of the front than behind it. In the outflow, $w_b < 0$ for most of the interval, reaching values as low as ~ -6 keV s^{-1} for short durations and $w_F > 0$, reaching values up to ~ 2 keV s^{-1} (Figure 1i2). The peak in w_F coincides with the peak in ~ 200 keV electron fluxes (Figure 1d2). Fermi acceleration and/or betatron cooling could therefore contribute to the observed energization in the outflow region behind the DF.

As presented above, the two DFs differ in typical features such as $\mathbf{B}$ and $\mathbf{V}_i$, as well as the high-energy electron fluxes observed at them. Betatron and Fermi acceleration can also be dominant in different regions around the front, evidencing a large variety of electron energization scenarios across different events, for electrons ahead and behind the front. We therefore need to statistically study the contribution of the betatron and Fermi mechanisms over a database of such DFs, for the pre-existing PS and outflow electrons.

4. Superposed Epoch Analysis of Acceleration at Dipolarization Fronts

4.1. Selected Events and Processing

We study the Fermi and betatron acceleration for a set of DFs with a single, sharp B_z increase and Earthward ion flows from Richard et al. (2022). We require burst-mode data from all four spacecraft to calculate the acceleration terms (Section 3.1). From a total of 250 events in the database, we find 78 DFs that fulfill our criteria.

We rescale the time series with the DF time scale, estimated by fitting a hyperbolic tangent to the four-spacecraft average B_z (Fu et al., 2012; Richard et al., 2022):

$$B_{z,\mathrm{fit}} = \frac{a}{2}\tanh\left(\frac{t - t_{\mathrm{DF}}}{b/2}\right) + \left(c + \frac{a}{2}\right) \quad (5)$$

where b is the time scale, t_{DF} is the DF time, and a and c determine B_z behind and ahead of the DF, respectively. We set boundaries $|a| > 4$ nT, $b \leq 8$ s, similar to Fu et al. (2012), and initially choose t_{DF} as the time of maximum $\partial B_z/\partial t$. The time coordinate of each DF is centered around t_{DF} ($\bar{t} = t - t_{\mathrm{DF}}$) and rescaled with b, for the DF boundary to span the same time for all events. A rolling median window of ~900 ms, shorter than the database's mean time scale, $\langle b \rangle = (3.72 \pm 2.21)$ s is applied to the DES data, to smooth out high-frequency variations.

4.2. Results

The superposed epoch analysis of the 78 DFs is presented in Figure 2. The median B_z (Figure 2a) shows the high occurrence of magnetic dips preceding DFs, around $\bar{t} = -2b$, also found in previous studies (Runov et al., 2011; Z. Yao et al., 2013; Z. H. Yao et al., 2015). The median electron temperature anisotropy $T_\perp/T_\parallel$ (Figure 2b) is approximately 1, suggesting that thermal electrons are mostly isotropic around the DF. Nevertheless, we find events with perpendicular temperature anisotropy $\left(T_\perp/T_\parallel > 1\right)$ behind the DFs. As seen in Figure 2d, on average $\kappa > 3$ for both thermal and 100 keV electrons, so Equation 1 is applicable for most cases. The median w_b (red line in Figure 2e) increases in the magnetic dip ahead of the DF, and peaks at the steep-B_z region. This is due to the increase in the convective derivative of **B** (Figure S4d in Supporting Information S1) just ahead of the DF. Around the B_z maximum, w_F (black line in Figure 2e) increases and retains its positive value $\left(\sim 0.03 \text{ keV s}^{-1}\right)$ behind the DF, until $\bar{t} \sim 6\ b$. In the outflow region, even though κ_{curv} is low, u_{E} increases, resulting in the large w_F (Figures S4f–S4g in Supporting Information S1). Therefore, w_b is dominant ahead of DFs, while w_F increases in the BBF behind the DFs, and on larger spatial scales.

The medians of normalized omnidirectional differential energy/particle fluxes from FPI/FEEPS (Figure 2f) show distinct features between near-thermal (1.1 keV) and suprathermal electrons. The 1.1 keV electron flux rapidly drops across the DF, maintaining a low value in the outflow region. High-energy omnidirectional fluxes start to increase ahead of the DF and peak in the Fermi-dominated region behind it, consistent with a similar increase in >10 keV electrons found by Runov et al. (2011).

To evaluate median ratios of perpendicular-to-parallel electron fluxes from FPI, we calculate $\log_{10} F_\perp/F_\parallel$, where $F_\perp = F_{90^\circ}$ and $F_\parallel = (F_{0^\circ} + F_{180^\circ})/2$ (Figure 2g). Parallel (F_{0°), antiparallel (F_{180°), and perpendicular (F_{90°) fluxes are defined between 0°–20°, 160°–180°, and 80°–100° pitch-angles, respectively. Low-energy, near-thermal electrons (1.1 keV in Figure 2g) are mostly moving along the magnetic field. Even though suprathermal electrons (16.1 keV and 27.5 keV) are mostly isotropic away from the DF, they exhibit a perpendicular anisotropy in the magnetic dip ahead of it, and in the flux pile-up region behind it.

5. Spatial Distribution of Acceleration Mechanisms and Energetic Electrons

For each DF from Section 4.2, we obtain median quantities in the PS and outflow intervals. We therefore need to differentiate between the different plasma environments in the two regions. We define the crossing from the dense pre-existing PS to the tenuous outflow as the time t_{n_e} of maximum $\partial n_e/\partial t$ (vertical dashed black line in Figure 2). We choose $\bar{t} \in [-2, t_{n_e}]\, b$ and $\bar{t} \in [t_{n_e}, 6]\, b$ as the pre-DF (ahead) and post-DF (behind) intervals, respectively, based on the median extent of w_b and w_F from Figure 2e.

The comparison between w_b and w_F ahead and behind the DFs (Figure 3b), shows that the pre-DF region is dominated by w_b, while the post-DF region is dominated by w_F. This is consistent with our previous result in Figure 2e. In the pre-DF region, we observe events with large values of $w_F < 0$, indicating Fermi deceleration of pre-existing PS electrons, although their number is small and thus do not contribute to the median w_F in our epoch analysis (Figure 2). This Fermi deceleration could be a result of the convecting BBF flow bending the flux tubes encountered in the pre-existing PS ($\mathbf{u}_E \cdot \boldsymbol{\kappa}_{curv} < 0$), previously shown in simulations (Chen & Wolf, 1999; Ugai, 2009).

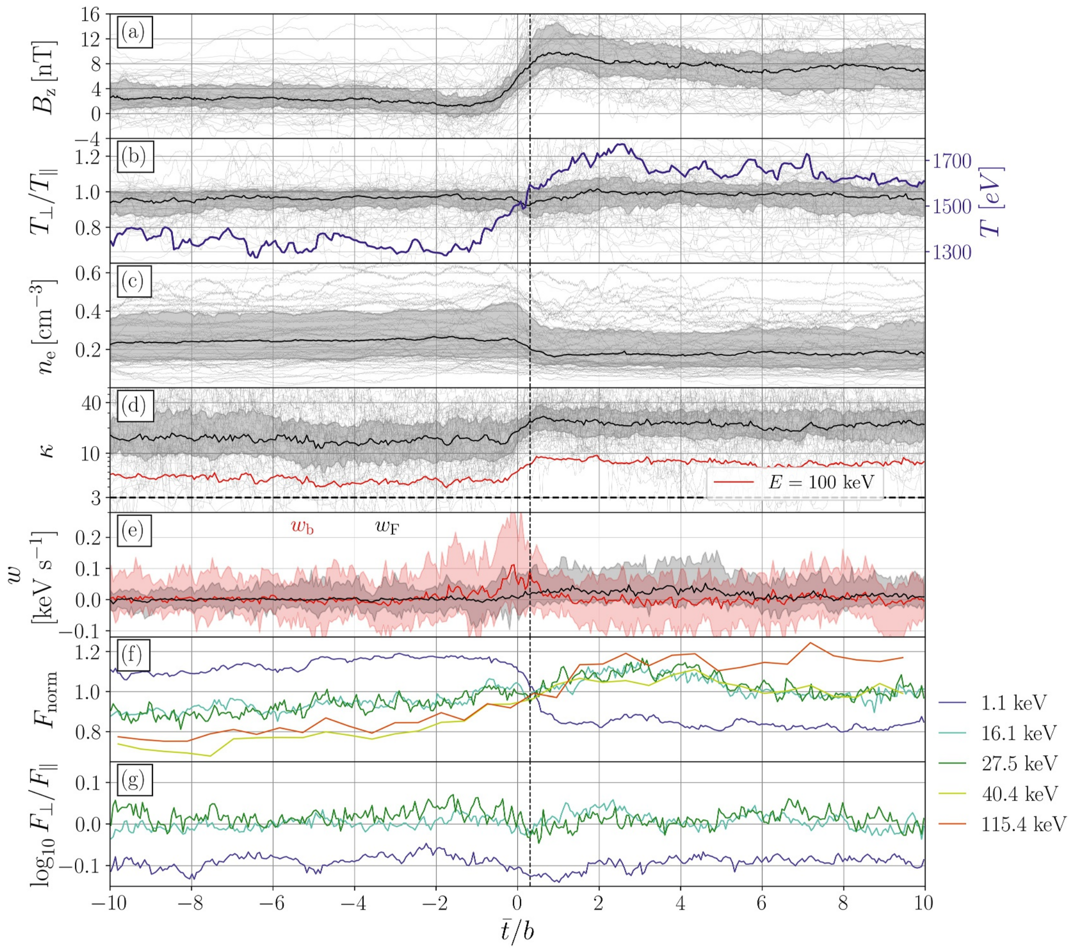

Figure 2. Superposed epoch analysis of 78 DFs. Gray lines in panels (a)–(d) show individual events. Solid lines represent median values. In panels (a)–(e), interquartile ranges are shown as shaded areas. (a) Magnetic field B_z component in geocentric solar magnetic. (b) Electron temperature anisotropy $T_\perp/T_\parallel$ and total temperature T (blue). (c) Electron number density n_e. (d) κ for thermal (black and gray lines) and median for 100 keV (red) electrons. Electrons are adiabatic above $\kappa = 3$ (dashed black line). (e) Medians of betatron (red) and Fermi (black) acceleration terms. (f) Medians of omnidirectional differential energy fluxes (normalized with the mean in flux in each interval) for three fast plasma investigation (FPI) (1.1, 16.1, and 27.5 keV) and differential particle fluxes for two fly's eye energetic particle spectrometer (40.4 and 115.4 keV) energy channels. (g) Electron perpendicular to parallel flux ratios for the three FPI energies used in panel (f). The vertical dashed black line indicates the time t_{n_e} of maximum $\partial n_e/\partial t$.

We find that w_b and w_F are dominant ahead and behind the DFs, respectively (Figure 3b). Therefore, we will focus on the relative importance of w_b and w_F in their respective regions of dominance. We study the distribution of w_b and w_F as functions of the DFs' distance from the center of the PS. To estimate the distance from the center of the PS, we use B_{xy}/B_{lobe}, as a proxy, where $B_{xy} = \sqrt{B_x^2 + B_y^2}$ and B_{lobe} is the lobe magnetic field, calculated by the pressure balance between the PS and the lobes (Asano et al., 2003). Near the lobe $B_{xy}/B_{\text{lobe}} \approx 1$, while $B_{xy}/B_{\text{lobe}} \approx 0$ near the center of the PS. For each DF, we calculate the median B_{xy}/B_{lobe} during the unperturbed PS interval, $\bar{t} \in [-10, -4]b$, based on Figure 2. With a few exceptions, we find that w_b and w_F increase toward the PS center ($B_{xy}/B_{\text{lobe}} \leq 0.3$), or equivalently, decrease toward the lobes (Figure 3a). The largest acceleration terms close to the center of the PS correspond to betatron acceleration.

Figures 3c–3e show w_b, w_F, $T_\perp/T_\parallel$, and $\log_{10}(F_\perp/F_\parallel)$ for 27.5 keV electrons as functions of distance from the Earth. Pre-DF w_b increases with distance ($X_{\text{GSM}} < -15\ R_E$), while the post-DF w_F increases toward the Earth, at $X_{\text{GSM}} > -21\ R_E$ (Figure 3c). The electron temperature (Figure 3d) ahead of the DFs is mostly isotropic and, in some cases, shows parallel anisotropy, while behind (black dots) we observe perpendicular anisotropy in some

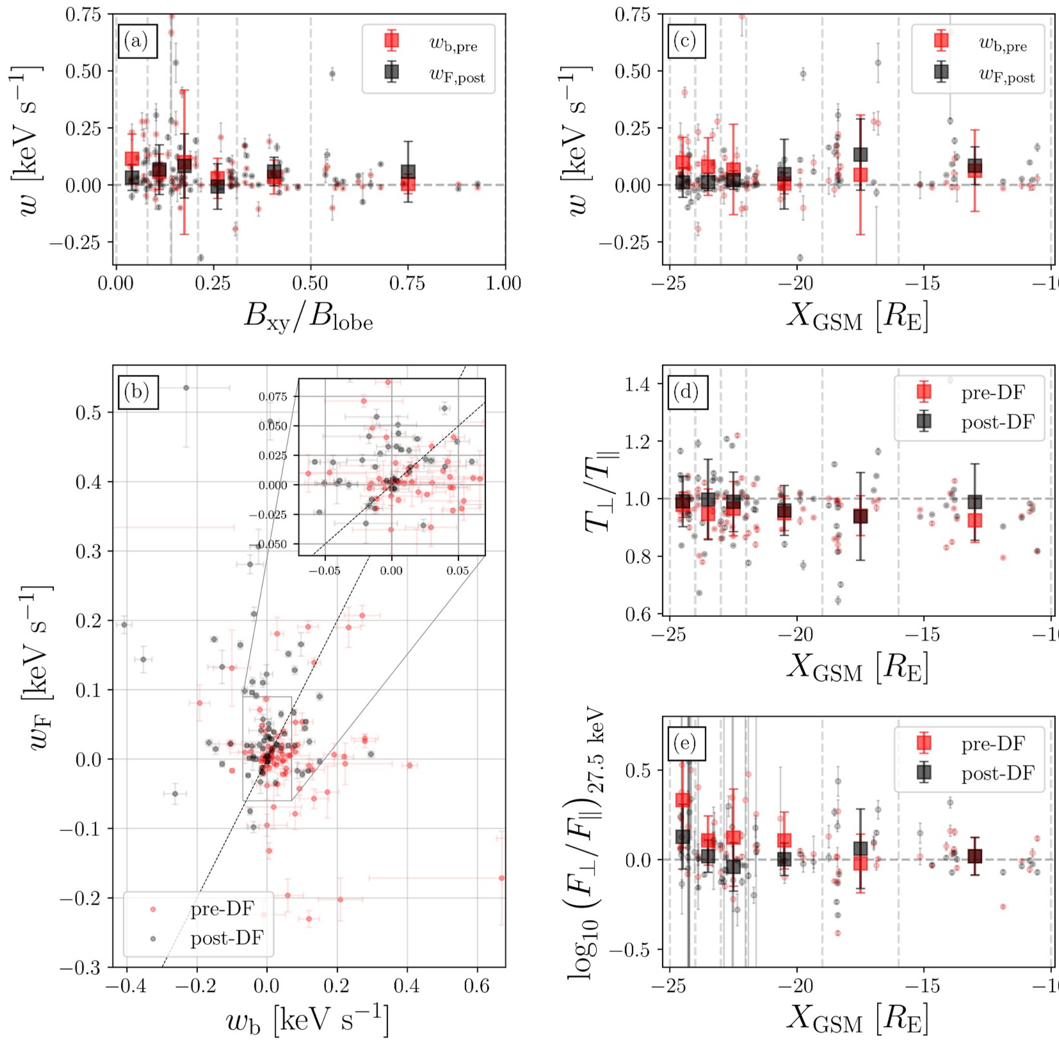

Figure 3. Spatial distribution of w_b and w_F and relative importance ahead and behind the DFs. Median quantities (transparent points) and binned over spatial dimensions (opaque squares) ahead and behind of DFs. Error bars of data points are the standard errors of the median. Error bars of binned values represent the standard deviation. The binning has been done such that each bin contains at least 10 data points. (a) The median w_b ahead (red) and w_F behind (black) the DFs as a function of distance from the center of the plasma sheet B_{xy}/B_{lobe}. (b) Comparison between median w_b and w_F ahead (red) and behind (red) the DFs. (c) Similar to (a) as a function of X_{GSM}. (d) Electron temperature anisotropy ratio $T_\perp/T_\parallel$ and (e) electron flux anisotropy for the highest fast plasma investigation energy channel as a function of X_{GSM}. Vertical dashed gray lines indicate the bins used.

events at $X_{GSM} < -20\ R_E$. However, there is no parallel/perpendicular temperature anisotropy that correlates with the increase of the Fermi/betatron term. This is expected, as the two acceleration mechanisms are more efficient for high-energy electrons. Even though there is no near-Earth apparent anisotropy for high-energy electrons, the perpendicular anisotropy becomes pronounced at large distances ($-25\ R_E \leq X_{GSM} \leq -20\ R_E$), as seen in Figure 3e. This is correlated with the increase in w_b ahead of DFs for $X_{GSM} < -15\ R_E$, suggesting that betatron acceleration is efficient at energizing electrons farther out in the magnetotail.

6. Discussion

Our analysis shows that w_b is dominant ahead of the DF, from the magnetic dip (due to the local $\partial B/\partial t \neq 0$) until the DF encounter, where B increases (Figure 2e). This increase of w_b at the DF has also been found by Ma et al. (2020). We also showed that high-energy perpendicular anisotropies are statistically present in the betatron-dominated region (Figure 2g). Gabrielse et al. (2016) found that drifting electrons in the pre-existing PS can be rapidly accelerated by the local $\partial B/\partial t > 0$ encountered at the arriving DF. Additionally, it was shown by simulations (C. Huang et al., 2015), that the most extreme electron acceleration in the pre-DF region is perpendicular to the magnetic field, facilitated by trapping of electrons by parallel electric fields, as the DF moves Earthwards. Our results support this picture of local betatron acceleration of trapped electrons ahead of DFs.

Behind the DFs, w_F is dominant, despite its small value, which is retained until $\bar{t} \sim 6$ b. Using the mean ion bulk speed, this timescale corresponds to a distance of $\sim$20 d_i in the outflow, where d_i is the ion inertial length calculated behind the DFs. The high-energy electrons observed behind the DFs could be attributed to Fermi acceleration through multiple passes through this region. A thermal electron with $T_\parallel \approx 2$ keV, has a parallel thermal velocity of $v_{\mathrm{th},\parallel} = \sqrt{2k_B T_\parallel/m_e} \approx 27 \times 10^3$ km s^{-1}. For a DF north-south size of $h_{\mathrm{DF}} \sim 2$ R_E, typical of BBFs (Nakamura et al., 2004), such an electron needs $\Delta t \approx h_{\mathrm{DF}}/v_{\mathrm{th},\parallel} \approx 0.46$ s to cross the acceleration region. With a constant kinetic energy change of $w_F \approx 0.17$ keV s^{-1} (maximum of the upper quartile in Figure 2e) over the crossing, the gain in parallel energy is $\Delta\mathcal{E}_\parallel \approx 0.1$ keV. From Equation 1, it follows that $w_F \propto \mathcal{E}_\parallel$, therefore, electrons with suprathermal $\mathcal{E}_\parallel$ would experience larger w_F (Equation 1), and reach much higher energies after multiple passes through the acceleration region. This cumulative acceleration suggests that Fermi acceleration contributes to extreme electron energization at DFs on large spatial scales.

We point out that the observed PADs are not necessarily a result of local acceleration at the DF alone, but also processes taking place in the reconnection region and during transport toward the DF. Therefore, the calculated w_b and w_F only provide us with information about the local contribution of the betatron and Fermi acceleration mechanisms. Even though our statistical results suggest that betatron and Fermi acceleration are dominant ahead and behind DFs, respectively, individual events can exhibit different behaviors. For example, Vaivads et al. (2021) interpreted large perpendicular electron fluxes in the flux pile-up region behind DFs and parallel fluxes ahead of them as the results of betatron and Fermi acceleration, respectively. Such events are also observed (Figure 2b) in our study, although they are statistically less likely over our database.

We find that perpendicular electron temperature and high-energy flux anisotropies in the outflow region behind DFs are statistically present (Figures 2d and 2f). These anisotropies, previously observed behind DFs (Khotyaintsev et al., 2011), are associated with a high occurrence of whistler-mode waves (Viberg et al., 2014). Because of the fast time-scales at which the whistlers reduce the anisotropy and quench the instability, these observations were interpreted as a signature of active betatron acceleration maintaining the anisotropy. We find that w_b is not significant behind DFs compared to w_F (Figure 2e). Nevertheless, $w_b > 0$ in a short time interval in the outflow, up until the flattening of B_z. This could be a region of whistler wave generation. A detailed comparison between whistler waves generated behind DFs and the electron betatron acceleration will be conducted in a future study.

The high w_b and perpendicular fluxes at distances of $X_{\mathrm{GSM}} < -20$ R_E are consistent with previous studies (Wu et al., 2013), showing that due to large outflow velocities early on in the jet's evolution, there is increased flux tube compression. Since the statistically most probable reconnection X-line is beyond ~ -20 R_E (Nagai, 2006; Nagai et al., 2023; Richard et al., 2022), betatron-dominated DFs at large X_{GSM} distances in our study could be attributed to more recently formed reconnection outflows. On the other hand, near Earth ($X_{\mathrm{GSM}} > -20$ R_E), the jet is slowed down in the more dipolarized region (Schmid et al., 2015); the field lines the outflow is convecting to are becoming shorter, and therefore, Fermi acceleration (possibly of type A) increases. We note here that we do not find a correlation between the outflow speed and the acceleration terms or X_{GSM} in our data set (not shown). Through simulations, K. Huang et al. (2021) showed that Earthward-propagating DFs form pancake, rolling-pin, and cigar PADs in sequence, consistent with an early stage betatron acceleration and transition to a near-Earth Fermi acceleration. Similarly, Birn et al. (2014) found perpendicular electron anisotropies to be present farther out in the magnetotail, while parallel anisotropies dominated near Earth. The findings of these simulation studies are consistent with our results for the distributions of w_b and w_F with distance from the Earth.

The distributions of w_b and w_F with distance from the center of the PS suggest that betatron acceleration can be more efficient near its center. Due to the magnetic field difference between DFs and the neutral sheet being larger than that between DFs and the near-lobe region, we expect w_b to be greater near the center of the PS. Even though a similar trend is found for w_F, a few high-w_F events occur for larger B_{xy}/B_{lobe}. Those could be a result of high-$\mathcal{E}_\parallel$ (large $w_F \propto \mathcal{E}_\parallel$, from Equation 1) electrons having their mirror points farther away from the center of the PS. In DF case studies, Runov et al. (2013) found pancake and cigar PADs near the neutral plane and away from it, respectively. Studying >40 keV PS electron fluxes, Åsnes et al. (2008) found a weak trend of perpendicular electron anisotropies occurring near the center of the PS, while parallel ones are more likely to appear at larger distances from the center. The results of Birn et al. (2014) show an increase in the occurrence of parallel electron anisotropies for larger distances from the central PS, while parallel electrons at that region in Birn et al. (2022) were found to originate from the PS boundary layer. Even though more cases with large B_{xy}/B_{lobe} would be needed to confirm these trends, our results show a similar distribution for w_b and w_F.

7. Conclusions

We studied the local betatron and Fermi electron acceleration in magnetotail reconnection DFs, using multi-spacecraft MMS observations. We conducted a statistical analysis of the rate of change of electron kinetic energy based on the guiding-center theory (Dahlin et al., 2014; Northrop, 1963) and their spatial distribution at 78 DFs. Our conclusions are the following:

- The betatron rate is dominant ahead of DFs, where suprathermal perpendicular electrons (up to ∼30 keV) are observed, suggesting local acceleration by the betatron mechanism. Fermi acceleration is dominant in the outflow, up to ∼20 d_i behind the DFs, where the most energetic electrons (a few 100 s keV) are detected.
- Most events with large rates of energy change due to betatron and Fermi acceleration are situated near the center of the PS. Events with significant Fermi acceleration can also be found closer to the lobes.
- Betatron acceleration and high-energy perpendicular electron fluxes are intensified farther tailward, closer to the most probable X-line location, likely corresponding to DFs early in their evolution. Fermi-dominated events are observed more frequently closer to Earth, where field-line shortening intensifies near Earth's dipole field.

Conflict of Interest

The authors declare no conflicts of interest relevant to this study.

Availability Statement

Magnetospheric multiscale data are available at https://lasp.colorado.edu/mms/sdc/public/data/. Data analysis was performed using the pyrfu analysis package (Richard et al., 2024). The scripts required to generate the figures in this paper are available at https://doi.org/10.5281/zenodo.19181971 (Kolokotronis, 2026).

Acknowledgments

This project received funding from the Knut and Alice Wallenberg Foundation (Grant KAW 2022.0087). C.N. was supported by the Swedish National Space Agency (SNSA) under Grant 2022-00121 and the Research Council of Norway under Contract No. 300865.

References

Angelopoulos, V., Baumjohann, W., Kennel, C. F., Coroniti, F. V., Kivelson, M. G., Pellat, R., et al. (1992). Bursty bulk flows in the inner central plasma sheet. *Journal of Geophysical Research*, *97*(A4), 4027–4039. https://doi.org/10.1029/91JA02701

Asano, Y., Mukai, T., Hoshino, M., Saito, Y., Hayakawa, H., & Nagai, T. (2003). Evolution of the thin current sheet in a substorm observed by geotail. *Journal of Geophysical Research*, *108*(A5), 1189. https://doi.org/10.1029/2002JA009785

Asano, Y., Shinohara, I., Retinò, A., Daly, P. W., Kronberg, E. A., Takada, T., et al. (2010). Electron acceleration signatures in the magnetotail associated with substorms. *Journal of Geophysical Research*, *115*(A5), A05215. https://doi.org/10.1029/2009JA014587

Ashour-Abdalla, M., El-Alaoui, M., Goldstein, M. L., Zhou, M., Schriver, D., Richard, R., et al. (2011). Observations and simulations of non-local acceleration of electrons in magnetotail magnetic reconnection events. *Nature Physics*, *7*(4), 360–365. https://doi.org/10.1038/nphys1903

Åsnes, A., Friedel, R. W. H., Lavraud, B., Reeves, G. D., Taylor, M. G. G. T., & Daly, P. (2008). Statistical properties of tail plasma sheet electrons above 40 keV. *Journal of Geophysical Research*, *113*(A3), A03202. https://doi.org/10.1029/2007JA012502

Baumjohann, W., & Treumann, R. A. (2006). In *Basic space plasma physics* (Reprinted ed.). Imperial College Press.

Birmingham, T. J. (1984). Pitch angle diffusion in the Jovian magnetodisc. *Journal of Geophysical Research*, *89*(A5), 2699–2707. https://doi.org/10.1029/JA089iA05p02699

Birn, J., Artemyev, A. V., Baker, D. N., Echim, M., Hoshino, M., & Zelenyi, L. M. (2012). Particle acceleration in the magnetotail and Aurora. *Space Science Reviews*, *173*(1–4), 49–102. https://doi.org/10.1007/s11214-012-9874-4

Birn, J., Hesse, M., Nakamura, R., & Zaharia, S. (2013). Particle acceleration in dipolarization events. *Journal of Geophysical Research: Space Physics*, *118*(5), 1960–1971. https://doi.org/10.1002/jgra.50132

Birn, J., Hesse, M., & Runov, A. (2022). Electron anisotropies in magnetotail dipolarization events. *Frontiers in Astronomy and Space Sciences*, *9*, 908730. https://doi.org/10.3389/fspas.2022.908730

Birn, J., Runov, A., & Hesse, M. (2014). Energetic electrons in dipolarization events: Spatial properties and anisotropy. *Journal of Geophysical Research: Space Physics*, *119*(5), 3604–3616. https://doi.org/10.1002/2013JA019738

Birn, J., Thomsen, M. F., & Hesse, M. (2004). Electron acceleration in the dynamic magnetotail: Test particle orbits in three-dimensional magnetohydrodynamic simulation fields. *Physics of Plasmas*, *11*(5), 1825–1833. https://doi.org/10.1063/1.1704641

Blake, J. B., Mauk, B. H., Baker, D. N., Carranza, P., Clemmons, J. H., Craft, J., et al. (2016). The Fly's eye energetic particle spectrometer (FEEPS) sensors for the magnetospheric multiscale (MMS) mission. *Space Science Reviews*, *199*(1), 309–329. https://doi.org/10.1007/s11214-015-0163-x

Büchner, J., & Zelenyi, L. M. (1989). Regular and chaotic charged particle motion in magnetotaillike field reversals: 1. Basic theory of trapped motion. *Journal of Geophysical Research*, *94*(A9), 11821–11842. https://doi.org/10.1029/JA094iA09p11821

Burch, J. L., Giles, B. L., Ahmadi, N., Argall, M. R., Baker, D. N., Blake, J. B., et al. (2024). Magnetospheric multiscale (mms) – Calibration and measurement algorithms document (cmad). *Space Physics Data Facility*. https://doi.org/10.48322/VSHD-SV21

Burch, J. L., Moore, T. E., Torbert, R. B., & Giles, B. L. (2016). Magnetospheric multiscale overview and science objectives. *Space Science Reviews*, *199*(1–4), 5–21. https://doi.org/10.1007/s11214-015-0164-9

Chen, C. X., & Wolf, R. A. (1999). Theory of thin-filament motion in Earth's magnetotail and its application to bursty bulk flows. *Journal of Geophysical Research*, *104*(A7), 14613–14626. https://doi.org/10.1029/1999JA900005

Dahlin, J. T., Drake, J. F., & Swisdak, M. (2014). The mechanisms of electron heating and acceleration during magnetic reconnection. *Physics of Plasmas*, *21*(9), 092304. https://doi.org/10.1063/1.4894484

Dahlin, J. T., Drake, J. F., & Swisdak, M. (2016). Parallel electric fields are inefficient drivers of energetic electrons in magnetic reconnection. *Physics of Plasmas*, *23*(12), 120704. https://doi.org/10.1063/1.4972082

Dunlop, M. W., Balogh, A., Glassmeier, K.-H., & Robert, P. (2002). Four-point cluster application of magnetic field analysis tools: The curlometer. *Journal of Geophysical Research*, *107*(A11), SMP23–1–SMP23–14. https://doi.org/10.1029/2001JA005088

Ergun, R. E., Tucker, S., Westfall, J., Goodrich, K. A., Malaspina, D. M., Summers, D., et al. (2016). The axial double probe and fields signal processing for the MMS mission. *Space Science Reviews*, *199*(1), 167–188. https://doi.org/10.1007/s11214-014-0115-x

Fu, H. S., Khotyaintsev, Y. V., André, M., & Vaivads, A. (2011). Fermi and betatron acceleration of suprathermal electrons behind dipolarization fronts. *Geophysical Research Letters*, *38*(16), L16104. https://doi.org/10.1029/2011GL048528

Fu, H. S., Khotyaintsev, Y. V., Vaivads, A., André, M., & Huang, S. Y. (2012). Occurrence rate of earthward-propagating dipolarization fronts. *Geophysical Research Letters*, *39*(10), L10101. https://doi.org/10.1029/2012GL051784

Fu, H. S., Khotyaintsev, Y. V., Vaivads, A., Retinò, A., & André, M. (2013). Energetic electron acceleration by unsteady magnetic reconnection. *Nature Physics*, *9*(7), 426–430. https://doi.org/10.1038/nphys2664

Gabrielse, C., Harris, C., Angelopoulos, V., Artemyev, A., & Runov, A. (2016). The role of localized inductive electric fields in electron injections around dipolarizing flux bundles. *Journal of Geophysical Research: Space Physics*, *121*(10), 9560–9585. https://doi.org/10.1002/2016JA023061

Gershman, D. J., Avanov, L. A., Boardsen, S. A., Dorelli, J. C., Gliese, U., Barrie, A. C., et al. (2017). Spacecraft and instrument photoelectrons measured by the dual electron spectrometers on MMS. *Journal of Geophysical Research: Space Physics*, *122*(11), 11548–11558. https://doi.org/10.1002/2017JA024518

Huang, C., Wu, M., Lu, Q., Wang, R., & Wang, S. (2015a). Electron acceleration in the dipolarization front driven by magnetic reconnection. *Journal of Geophysical Research: Space Physics*, *120*(3), 1759–1765. https://doi.org/10.1002/2014JA020918

Huang, K., Lu, Q., Lu, S., Wang, R., & Wang, S. (2021). Formation of pancake, rolling pin, and cigar distributions of energetic electrons at the dipolarization fronts (DFs) driven by magnetic reconnection: A two-dimensional particle-in-cell simulation. *Journal of Geophysical Research: Space Physics*, *126*(10), e2021JA029939. https://doi.org/10.1029/2021JA029939

Huang, S. Y., Fu, H. S., Yuan, Z. G., Zhou, M., Fu, S., Deng, X. H., et al. (2015b). Electromagnetic energy conversion at dipolarization fronts: Multispacecraft results. *Journal of Geophysical Research: Space Physics*, *120*(6), 4496–4502. https://doi.org/10.1002/2015JA021083

Khotyaintsev, Y. V., Cully, C. M., Vaivads, A., André, M., & Owen, C. J. (2011). Plasma jet braking: Energy dissipation and nonadiabatic electrons. *Physical Review Letters*, *106*(16), 165001. https://doi.org/10.1103/PhysRevLett.106.165001

Kolokotronis, A. (2026). *Statistical study of betatron and fermi electron acceleration at dipolarization fronts (v1.0.1)*. Zenodo. https://doi.org/10.5281/zenodo.19181971

Lindqvist, P.-A., Olsson, G., Torbert, R. B., King, B., Granoff, M., Rau, D., et al. (2016). The spin-plane double probe electric field instrument for MMS. *Space Science Reviews*, *199*(1), 137–165. https://doi.org/10.1007/s11214-014-0116-9

Liu, C. M., Fu, H. S., Xu, Y., Cao, J. B., & Liu, W. L. (2017). Explaining the rolling-pin distribution of suprathermal electrons behind dipolarization fronts. *Geophysical Research Letters*, *44*(13), 6492–6499. https://doi.org/10.1002/2017GL074029

Ma, W., Zhou, M., Zhong, Z., & Deng, X. (2020). Electron acceleration rate at dipolarization fronts. *Astrophysical Journal*, *903*(2), 84. https://doi.org/10.3847/1538-4357/abb8cc

Ma, W., Zhou, M., Zhong, Z., & Deng, X. (2022). Contrasting the mechanisms of reconnection-driven electron acceleration with in situ observations from MMS in the terrestrial magnetotail. *Astrophysical Journal*, *931*(2), 135. https://doi.org/10.3847/1538-4357/ac6be6

Malykhin, A., Grigorenko, E., Kronberg, E., & Daly, P. (2018). The effect of the betatron mechanism on the dynamics of superthermal electron fluxes within dipolizations in the magnetotail. *Geomagnetism and Aeronomy*, *58*(6), 744–752. https://doi.org/10.1134/S0016793218060099

Nagai, T. (2006). Location of magnetic reconnection in the magnetotail. *Space Science Reviews*, *122*(1), 39–54. https://doi.org/10.1007/s11214-006-6216-4

Nagai, T., Shinohara, I., Saito, Y., Ieda, A., & Nakamura, R. (2023). Location and timing of magnetic reconnections in earth's magnetotail: Accomplishments of the 29-Year geotail near-earth magnetotail survey. *Journal of Geophysical Research: Space Physics*, *128*(12), e2023JA032023. https://doi.org/10.1029/2023JA032023

Nakamura, R., Baumjohann, W., Klecker, B., Bogdanova, Y., Balogh, A., Rème, H., et al. (2002). Motion of the dipolarization front during a flow burst event observed by cluster. *Geophysical Research Letters*, *29*(20), 3–1–3–4. https://doi.org/10.1029/2002GL015763

Nakamura, R., Baumjohann, W., Mouikis, C., Kistler, L. M., Runov, A., Volwerk, M., et al. (2004). Spatial scale of high-speed flows in the plasma sheet observed by Cluster. *Geophysical Research Letters*, *31*(9), L09804. https://doi.org/10.1029/2004GL019558

Northrop, T. G. (1963). Adiabatic charged-particle motion. *Reviews of Geophysics*, *1*(3), 283–304. https://doi.org/10.1029/RG001i003p00283

Pan, Q., Ashour-Abdalla, M., El-Alaoui, M., Walker, R. J., & Goldstein, M. L. (2012). Adiabatic acceleration of suprathermal electrons associated with dipolarization fronts. *Journal of Geophysical Research*, *117*(A12), A12224. https://doi.org/10.1029/2012JA018156

Pollock, C., Moore, T., Jacques, A., Burch, J., Gliese, U., Saito, Y., et al. (2016). Fast plasma investigation for magnetospheric multiscale. *Space Science Reviews*, *199*(1), 331–406. https://doi.org/10.1007/s11214-016-0245-4

Richard, L., Khotyaintsev, Y. V., Graham, D. B., & Russell, C. T. (2022). Are dipolarization fronts a typical feature of magnetotail plasma jets fronts? *Geophysical Research Letters*, *49*(22), e2022GL101693. https://doi.org/10.1029/2022GL101693

Richard, L., Khotyaintsev, Y. V., Vaivads, A., Graham, D. B., Norgren, C., & Johlander, A. (2024). Python rymdfysik utilities (pyrfu): An open-source python package for advanced in-situ space plasma analysis. *Zenodo*. https://doi.org/10.5281/zenodo.10678695

Runov, A., Angelopoulos, V., Gabrielse, C., Zhou, X.-Z., Turner, D., & Plaschke, F. (2013). Electron fluxes and pitch-angle distributions at dipolarization fronts: THEMIS multipoint observations. *Journal of Geophysical Research: Space Physics*, *118*(2), 744–755. https://doi.org/10.1002/jgra.50121

Runov, A., Angelopoulos, V., Zhou, X.-Z., Zhang, X.-J., Li, S., Plaschke, F., & Bonnell, J. (2011). A THEMIS multicase study of dipolarization fronts in the magnetotail plasma sheet. *Journal of Geophysical Research*, *116*(A5), A05216. https://doi.org/10.1029/2010JA016316

Russell, C. T., Anderson, B. J., Baumjohann, W., Bromund, K. R., Dearborn, D., Fischer, D., et al. (2016). The magnetospheric Multiscale magnetometers. *Space Science Reviews*, *199*(1), 189–256. https://doi.org/10.1007/s11214-014-0057-3

Schmid, D., Nakamura, R., Plaschke, F., Volwerk, M., & Baumjohann, W. (2015). Two states of magnetotail dipolarization fronts: A statistical study. *Journal of Geophysical Research: Space Physics*, *120*(2), 1096–1108. https://doi.org/10.1002/2014JA020380

Schmid, D., Volwerk, M., Nakamura, R., Baumjohann, W., & Heyn, M. (2011). A statistical and event study of magnetotail dipolarization fronts. *Annales Geophysicae*, *29*(9), 1537–1547. https://doi.org/10.5194/angeo-29-1537-2011

Sitnov, M. I., Swisdak, M., & Divin, A. V. (2009). Dipolarization fronts as a signature of transient reconnection in the magnetotail. *Journal of Geophysical Research*, *114*(A4), A04202. https://doi.org/10.1029/2008JA013980

Smets, R., Delcourt, D., Sauvaud, J. A., & Koperski, P. (1999). Electron pitch angle distributions following the dipolarization phase of a substorm: Interball-tail observations and modeling. *Journal of Geophysical Research*, *104*(A7), 14571–14581. https://doi.org/10.1029/1998JA900162

Steinvall, K., Richard, L., Fülöp, T., Hanebring, L., & Pusztai, I. (2025). Eulerian and Lagrangian electron energisation during magnetic reconnection. *Journal of Plasma Physics*, *91*(3), E90. https://doi.org/10.1017/S0022377825100408

Tang, C. L., Wang, X., & Zhou, M. (2021). Electron pitch angle distributions around dipolarization fronts at the off magnetic equator. *Journal of Geophysical Research: Space Physics*, *126*(2), e2020JA028787. https://doi.org/10.1029/2020JA028787

Turner, D. L., Fennell, J. F., Blake, J. B., Clemmons, J. H., Mauk, B. H., Cohen, I. J., et al. (2016). Energy limits of electron acceleration in the plasma sheet during substorms: A case study with the Magnetospheric Multiscale (MMS) mission. *Geophysical Research Letters*, *43*(15), 7785–7794. https://doi.org/10.1002/2016GL069691

Ugai, M. (2009). Fast reconnection evolution in an arcadelike magnetic loop structure. *Physics of Plasmas*, *16*(6), 062312. https://doi.org/10.1063/1.3158949

Vaivads, A., Khotyaintsev, Y. V., Retinò, A., Fu, H. S., Kronberg, E. A., & Daly, P. W. (2021). Cluster observations of energetic electron acceleration within earthward reconnection jet and associated magnetic flux rope. *Journal of Geophysical Research: Space Physics*, *126*(8), e2021JA029545. https://doi.org/10.1029/2021JA029545

Viberg, H., Khotyaintsev, Y. V., Vaivads, A., André, M., Fu, H. S., & Cornilleau-Wehrlin, N. (2014). Whistler mode waves at magnetotail dipolarization fronts. *JGR Space Physics*, *119*(4), 2605–2611. https://doi.org/10.1002/2014JA019892

Wei, Y. Y., Huang, S. Y., Jiang, K., Yuan, Z. G., Xu, S. B., Zhang, J., et al. (2023). Direct evidence of electron acceleration at the dipolarization front. *Astrophysical Journal*, *950*(2), 112. https://doi.org/10.3847/1538-4357/acd1dd

Wu, M., Lu, Q., Volwerk, M., Vörös, Z., Zhang, T., Shan, L., & Huang, C. (2013). A statistical study of electron acceleration behind the dipolarization fronts in the magnetotail. *Journal of Geophysical Research: Space Physics*, *118*(8), 4804–4810. https://doi.org/10.1002/jgra.50456

Xing, X., Liu, C., & Cao, J. (2023). Electron rolling-pin distributions preceding dipolarization fronts. *Geophysical Research Letters*, *50*(18), e2023GL105337. https://doi.org/10.1029/2023GL105337

Xu, Y., Fu, H. S., Liu, C. M., & Wang, T. Y. (2018). Electron acceleration by dipolarization fronts and magnetic reconnection: A quantitative comparison. *Astrophysical Journal*, *853*(1), 11. https://doi.org/10.3847/1538-4357/aa9f2f

Yao, Z., Sun, W. J., Fu, S. Y., Pu, Z. Y., Liu, J., Angelopoulos, V., et al. (2013). Current structures associated with dipolarization fronts. *Journal of Geophysical Research: Space Physics*, *118*(11), 6980–6985. https://doi.org/10.1002/2013JA019290

Yao, Z. H., Liu, J., Owen, C. J., Forsyth, C., Rae, I. J., Pu, Z. Y., et al. (2015). A physical explanation for the magnetic decrease ahead of dipolarization fronts. *Annales Geophysicae*, *33*(10), 1301–1309. https://doi.org/10.5194/angeo-33-1301-2015

Young, D. T., Burch, J. L., Gomez, R. G., De Los Santos, A., Miller, G. P., Wilson, P., et al. (2016). Hot plasma composition analyzer for the magnetospheric multiscale mission. *Space Science Reviews*, *199*(1), 407–470. https://doi.org/10.1007/s11214-014-0119-6

Zhong, Z., Zhou, M., Tang, R., Deng, X., Turner, D., Cohen, I., et al. (2020). Direct evidence for electron acceleration within ion-scale flux rope. *Geophysical Research Letters*, *47*(1), e2019GL085141. https://doi.org/10.1029/2019GL085141